

Semi-implicit Hybrid Discrete (\mathbf{H}_N^T) Approximation of Thermal Radiative Transfer

Ryan G. McClarren · James A. Rossmanith ·
Minwoo Shin*

Received: date / Accepted: date

Abstract The thermal radiative transfer (TRT) equations form an integro-differential system that describes the propagation and collisional interactions of photons. Computing accurate and efficient numerical solutions to TRT is challenging for several reasons, the first of which is that TRT is defined on a high-dimensional phase space that includes the independent variables of time, space, and velocity. In order to reduce the dimensionality of the phase space, classical approaches such as the P_N (spherical harmonics) or the S_N (discrete ordinates) ansatz are often used in the literature. In this work, we introduce a novel approach: the hybrid discrete (\mathbf{H}_N^T) approximation to the radiative thermal transfer equations. This approach acquires desirable properties of both P_N and S_N , and indeed reduces to each of these approximations in various limits: $\mathbf{H}_N^1 \equiv P_N$ and $\mathbf{H}_0^T \equiv S_T$. We prove that \mathbf{H}_N^T results in a system of hyperbolic partial differential equations for all $T \geq 1$ and $N \geq 0$. Another challenge in solving the TRT system is the inherent stiffness due to the large timescale separation between propagation and collisions, especially in the diffusive (i.e., highly collisional) regime. This stiffness challenge can be partially overcome via implicit time integration, although

* Corresponding Author

Ryan G. McClarren
University of Notre Dame
Department of Aerospace and Mechanical Engineering
Notre Dame, IN 46556, USA
E-mail: rmclarr@nd.edu

James A. Rossmanith
Iowa State University
Department of Mathematics
Ames, IA 50011-2104, USA
E-mail: rossmani@iastate.edu

Minwoo Shin
University of Notre Dame
Department of Aerospace and Mechanical Engineering
Notre Dame, IN 46556, USA
E-mail: mshin@nd.edu

fully implicit methods may become computationally expensive due to the strong non-linearity and system size. On the other hand, explicit time-stepping schemes that are not also asymptotic-preserving in the highly collisional limit require resolving the mean-free path between collisions, making such schemes prohibitively expensive. In this work we develop a numerical method that is based on a nodal discontinuous Galerkin discretization in space, coupled with a semi-implicit discretization in time. In particular, we make use of a second order explicit Runge-Kutta scheme for the streaming term and an implicit Euler scheme for the material coupling term. Furthermore, in order to solve the material energy equation implicitly after each predictor and corrector step, we linearize the temperature term using a Taylor expansion; this avoids the need for an iterative procedure, and therefore improves efficiency. In order to reduce unphysical oscillation, we apply a slope limiter after each time step. Finally, we conduct several numerical experiments to verify the accuracy, efficiency, and robustness of the H_N^T ansatz and the numerical discretizations.

Keywords thermal radiative transfer · discontinuous Galerkin · discrete hybrid approximation · semi-implicit time integration · asymptotic-preserving

Mathematics Subject Classification (2010) 85A25 · 65M60

1 Introduction

The thermal radiative transfer (TRT) equations describe the interaction of matter and thermal radiation, and are used in a wide range of applications including remote sensing, glass manufacturing, and combustion [31]. The TRT equations model the propagation, absorption, and emission of photons, as well as the coupling of these dynamics to background media via a material-energy equation. Accurate and efficient numerical solutions of the TRT equations are challenging for several reasons:

1. The TRT equations form an integro-differential system that is posed on a high-dimensional phase space: the time dimension, up to three spatial dimensions, two velocity direction dimensions, and a frequency dimension;
2. Optically thick media introduces stiffness due to the large timescale separation between propagation and collisions;
3. The material-energy coupling equation introduces strong non-linearity.

1.1 Discretization of the phase space

Two broad classes of solution approaches have been used to tackle the TRT equation (1) stochastic methods and (2) deterministic methods; each approach offers their own advantages and disadvantages. The main workhorse of the stochastic approach is the Monte Carlo (MC) method, which is considered one of the most reliable methods in the radiation community [8, 24, 36]. Monte Carlo methods produce statistical noise due to under-sampling of the phase space; and therefore, to compensate for this under-sampling, many MC histories are required, which in turns makes the MC calculation expensive. As a result, high performance computing approaches are needed. In the

realm of deterministic approaches the most popular methods are the discrete ordinates (S_N) method [3, 13, 14, 15, 16, 29] and the spherical harmonics (P_N) method [18, 21, 25, 26, 28]. The advantages of these approaches are that, relative to Monte Carlo, they are less computationally expensive. On the other hand they each suffer from their own specific disadvantages.

The S_N approximation scheme creates a system of equations along a discrete set of angular directions that are taken from a specific quadrature set [4, 10, 17, 33], and angular integrals are calculated via the given quadrature set. The S_N method has been the subject of intense research, and many large-scale efficient solution techniques have been developed, including approaches that have been shown to scale on leadership-class computers [1]. The S_N method's main drawback is the phenomenon known as ray effects [14, 15], which arises due to the fact that particles move only along certain directions in the quadrature set. These effects are conspicuously observed in optically thin materials with localized sources or sharp material discontinuities.

On the other hand, the P_N method approximates the solution with a spherical harmonics expansion that by construction is rotationally invariant and converges in the L^2 sense [9]. The main disadvantage of the P_N approach is that it is plagued by Gibbs phenomena (i.e., unphysical oscillations) due to the fact that it is a truncated spectral method and can thereby produce the negative particle concentrations [9, 22], which is physically undesirable. Additionally, in the P_N method, when N is small, the wave speeds are reduced because the system eigenvalues can be far from unity.

1.2 Stiffness

Another challenging aspect in accurately and efficiently solving the thermal radiative transfer (TRT) equations is that the system is inherently *stiff*. This stiffness is especially pervasive in the diffusive regime (i.e., highly collisional), where there is a large timescale separation between propagation and collisions. The reduction of the kinetic TRT system to a lower dimensional system of partial differential equations (PDEs) via an ansatz such as discrete ordinate (S_N) or spherical harmonics (P_N) does not alleviate this problem.

From the perspective of numerical methods, the stiffness challenge can be partially overcome via implicit time integration, although fully implicit methods may become computationally expensive due to the strong nonlinearity and system size. On the other hand, explicit time-stepping schemes that are not also asymptotic-preserving in the highly collisional limit require resolving the mean-free path between collisions, making such schemes prohibitively expensive.

An efficient alternative to both fully implicit and fully explicit schemes are semi-implicit schemes, where, at least roughly-speaking, the transport is handled explicitly, while the material coupling term (i.e., collisions) are handled implicitly. For example, Klar et al. [11, 12] developed and analyzed an operator splitting approach that was shown to be asymptotically-preserving while at the same time relatively efficient in all regimes. A different semi-implicit approach for TRT was subsequently developed by McClarren et al. [21], in which a two-stage second-order Runge-Kutta (RK) scheme was used for the streaming term and the backward Euler scheme was used for the

material coupling term. This scheme was also shown to be asymptotic-preserving in the diffusive limit.

1.3 Strong nonlinearity in the material coupling term

In the absence of material coupling, the thermal radiative transfer equations and its various reductions (e.g., P_N or S_N) represent a system of linear constant-coefficient partial differential equations. The presence of the material coupling term introduces strong nonlinearity. For explicit time-stepping methods this nonlinearity does not pose a direct challenge, although, as mentioned above, explicit methods will then suffer from small time-steps. For fully implicit time-stepping methods the nonlinearity results in large nonlinear algebraic equations that must be inverted in time-step, resulting in significant computational expense. For semi-implicit time-stepping approaches, a nonlinear material coupling term only introduces a local nonlinear algebraic equation (i.e., local on each element), although even this can add computational expense. Fortunately, McClarren, Evans, and Lowrie [21] showed that the local nonlinear problems presented by a semi-implicit approach can be linearized via a simple Taylor series argument. It was shown that this linearization reduces the computational complexity and does not adversely affect overall accuracy of the method.

1.4 Scope of this work

In order to address some of the shortcomings of classical deterministic methods, we introduce in this work the hybrid discrete (H_N^T) approximation, which hybridizes aspects of the P_N and S_N methods. The H_N^T approximation is equivalent to spherical harmonics (P_N) approximation when the number of the discretized velocity space (T) is one and only depends on the order of spherical harmonics basis functions (N). Also, it is equivalent to the discrete ordinate (S_N) method for a certain quadrature set. By hybridizing P_N and S_N , the H_N^T approximation is able to acquire beneficial properties of both of these classical approaches. We prove that H_N^T results in a system of hyperbolic partial differential equations for all $T \geq 1$ and $N \geq 0$.

Once we have shown how to reduce the TRT equations into their H_N^T approximate form, we will discretize the resulting PDE system via the same semi-implicit time integration scheme introduced by McClarren et al. [21]. In particular, this approach uses a second order Runge-Kutta explicit time discretization schemes for the streaming term and a backward Euler scheme for the material energy term; this allows us to resolve the stiffness of the TRT systems and to preserve the asymptotic diffusion limit. Furthermore, in order to solve the material energy equation implicitly after each predictor and corrector step, we linearize the temperature term using a Taylor expansion; this avoids the need for an iterative procedure, and therefore improves efficiency. In order to reduce unphysical oscillation, we apply a slope limiter after each time step.

In the present work we will consider only grey, i.e., frequency-averaged, radiation transport equations in slab geometry. Non-grey and multi-dimensional radiative

transfer will be studied in future work. For the grey TRT system in slab geometry we consider several standard test cases in order to validate the accuracy, efficiency, and robustness of scheme, as well as to highlight benefits over P_N and S_N solutions.

The remainder of this paper is organized as follows. In section 2 the novel hybrid discrete (H_N^T) approximations in slab geometry are derived and discussed. In section 3 we develop a semi-implicit nodal discontinuous Galerkin finite element scheme for the resulting H_N^T systems. In section 4 we provide numerical results of H_N^T approximations on various benchmark problems to show its robustness and asymptotic preserving property. Conclusions are presented in section 5.

2 Hybrid discrete approximation

In this section, we formulate H_N^T approximations to the radiative transfer in one-dimension. We begin with the thermal radiative transfer in slab geometry, and then derive the hybrid discrete approximation. We prove that the H_N^T system is always hyperbolic.

2.1 Frequency-independent grey thermal transfer

Consider the 1D scattering-free thermal radiative transfer equation (e.g., see [21]):

$$\frac{1}{c} \frac{\partial \widehat{I}}{\partial t} + \mu \frac{\partial \widehat{I}}{\partial z} + \widehat{\sigma} \widehat{I} = \widehat{\sigma} \widehat{B} + \widehat{s}, \quad (2.1)$$

where $\widehat{I}(t, z, \mu, \nu) : \mathbb{R}_{\geq 0} \times \mathbb{R} \times [-1, 1] \times \mathbb{R} \mapsto \mathbb{R}$ is the specific intensity, $t \in \mathbb{R}_{\geq 0}$ is time, $z \in \mathbb{R}$ is the spatial variable, $\mu \in [-1, 1]$ is the angular variable, i.e., $\mu = \cos \varphi$ with polar angle $\varphi \in [0, \pi]$, $\nu \in \mathbb{R}$ is the frequency of the photon, $\widehat{s}(t, z, \nu) : \mathbb{R}_{\geq 0} \times \mathbb{R} \times \mathbb{R} \mapsto \mathbb{R}$ is an external source term, $\widehat{\sigma}(z, \nu) : \mathbb{R} \times \mathbb{R} \mapsto \mathbb{R}_{\geq 0}$ is the opacity, $\widehat{B}(\nu, \theta) : \mathbb{R} \times \mathbb{R}_{\geq 0} \mapsto \mathbb{R}_{\geq 0}$ is the Planck function that satisfies:

$$B(\theta) := \int_{\nu} \widehat{B}(\nu, \theta) d\nu = \frac{ac\theta^4}{2}, \quad (2.2)$$

where $\theta(t, z) : \mathbb{R}_{\geq 0} \times \mathbb{R} \mapsto \mathbb{R}_{\geq 0}$ is the material temperature in keV, $c = 3 \times 10^{10} \text{ cm s}^{-1}$ is the speed of light, and $a = 1.372 \times 10^{14} \text{ ergs cm}^{-3} \text{ keV}^{-4}$ is the radiation constant. The notation $\widehat{\cdot}$ is used to signify quantities that depend explicitly on the frequency ν . Equation (2.1) couples to the material-energy equation:

$$\frac{\partial e}{\partial t} = \int_{\mu} \int_{\nu} \widehat{\sigma}(z, \nu) \left(\widehat{I}(t, z, \mu, \nu) - \widehat{B}(\nu, \theta) \right) d\nu d\mu, \quad (2.3)$$

where $e(\rho, \theta) : \mathbb{R}_{\geq 0} \times \mathbb{R}_{\geq 0} \mapsto \mathbb{R}_{\geq 0}$ is the material energy per volume and $\rho(t, z) : \mathbb{R}_{\geq 0} \times \mathbb{R} \mapsto \mathbb{R}_{\geq 0}$ is the material density.

For the remainder of this paper we consider only the case where the opacity is frequency independent: $\widehat{\sigma}(z, \nu) \rightarrow \sigma(z)$. In this approximation, we define the following frequency-integrated quantities (which now removes the $\widehat{\cdot}$ notation):

$$I(t, z, \mu) := \int_{\nu} \widehat{I}(t, z, \mu, \nu) d\nu, \quad s(t, z) := \int_{\nu} \widehat{s}(t, z, \nu) d\nu, \quad (2.4)$$

and equation (2.2). We also define the angular moment of the radiation intensity \widehat{I} as follows:

$$E(t, z) := \frac{1}{c} \int_{\mu} \int_{\nu} \widehat{I}(t, z, \mu, \nu) d\nu d\mu = \frac{1}{c} \int_{\mu} I(t, z, \mu) d\mu. \quad (2.5)$$

Furthermore, we will assume throughout this work that the material density, ρ , is constant, which results in the following:

$$\frac{\partial e}{\partial t} = \frac{\partial e}{\partial \theta} \frac{\partial \theta}{\partial t} + \frac{\partial e}{\partial \rho} \frac{\partial \rho}{\partial t} = C_v \frac{\partial \theta}{\partial t}, \quad (2.6)$$

where $C_v = 0.3 \times 10^{16} \text{erg/cm}^3 / \text{keV}$ is the heat capacity at constant volume.

Under the assumption of a frequency independent opacity and a constant material density, we can integrate (2.1) over the frequency ν and arrive at the following grey transport equation and material-energy equation:

$$\frac{1}{c} \frac{\partial I}{\partial t} + \mu \frac{\partial I}{\partial z} + \sigma I = \frac{1}{2} \sigma a c \theta^4 + \frac{s}{2}, \quad (2.7)$$

$$C_v \frac{\partial \theta}{\partial t} = \sigma \left(\int_{-1}^1 I(t, z, \mu) d\mu - a c \theta^4 \right). \quad (2.8)$$

respectively. These equations are defined on $t > 0$, $z \in (z_L, z_R)$, and $\mu \in [-1, 1]$, and must be equipped with initial conditions at $t = 0$ and appropriate boundary conditions at $z = z_L$ and $z = z_R$.

2.2 Formulation of the 1D H_N^T approximation

Equations (2.7)–(2.8) represent a integro-differential equation for the intensity, $I(t, z, \mu)$, and the material temperature, $\theta(t, z)$. There are two main classes of techniques for approximating such systems: (1) direct Monte-Carlo simulations and (2) dimension reduction via ansatz in μ . Standard techniques for reducing the dimensionality of these equations to a system defined only over (t, z) include the P_N (i.e., spherical harmonics) (e.g., see [2]) and S_N (i.e., discrete ordinates) [3] methods. Spherical harmonics (P_N) suffer from producing negative (and therefore unphysical) intensities, while discrete ordinates (S_N) suffer from ray effects. In this work we consider an alternative approach that was first developed in Shin [30], namely the H_N^T (i.e., hybrid discrete) approach. The main advantage of H_N^T is that it allows us to work with an approximation that combines desirable aspects of both P_N and S_N . In particular H_N^T reduces to each of these approximations in various limits: $H_N^1 \equiv P_N$ and $H_0^T \equiv S_T$.

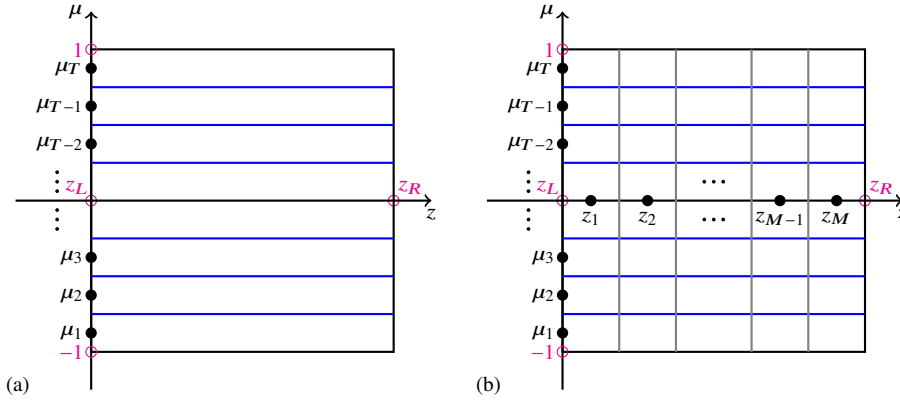


Fig. 2.1: The H_N^T approximation. Panel (a) shows the discrete velocity bands, each of which is centered at $\mu_j \in (-1, 1)$ for $j = 1, 2, \dots, m$. Panel (b) shows the discrete velocity bands with the physical z -mesh superimposed.

The H_N^T approximation of Shin [30] begins by constructing a mesh in velocity space. In 1D this means a mesh in the angular variables $\mu \in [-1, 1]$:

$$\bigcup_{j=1}^T \left[\mu_j - \frac{\Delta\mu}{2}, \mu_j + \frac{\Delta\mu}{2} \right], \quad \mu_j = -1 + \left(j - \frac{1}{2} \right) \Delta\mu, \quad \text{and} \quad \Delta\mu = \frac{2}{T}, \quad (2.9)$$

which we depict in Figure 2.1(a). With this velocity mesh, the H_N^T approach defines on the velocity band centered at μ_j the following band-localized intensity:

$$I(t, z, \mu(\alpha)) \Big|_{\mu \in \left[\mu_j - \frac{\Delta\mu}{2}, \mu_j + \frac{\Delta\mu}{2} \right]} \approx I^{(j)}(t, z, \alpha) := \sum_{k=0}^N \left(\frac{2k+1}{2} \right) u_k^{(j)}(t, z) p_k(\alpha), \quad (2.10)$$

for $j = 1, 2, \dots, T$, where $\alpha \in [-1, 1]$ is a local variable in each velocity band centered at μ_j with thickness $\Delta\mu$:

$$\mu(\alpha) = \mu_j + \alpha \left(\frac{\Delta\mu}{2} \right), \quad (2.11)$$

and $p_k(\alpha)$ is the k^{th} order Legendre polynomial:

$$p_k(\alpha) = \left(\frac{2k-1}{k} \right) \alpha p_{k-1}(\alpha) - \left(\frac{k-1}{k} \right) p_{k-2}(\alpha), \quad p_0(\alpha) = 1, \quad p_1(\alpha) = \alpha, \quad (2.12)$$

and $\int_{-1}^1 p_k(\alpha) p_m(\alpha) d\alpha = \left(\frac{2}{2k+1} \right) \delta_{km}.$

The moments in (2.10) are defined as

$$u_k^{(j)}(t, z) = \int_{-1}^1 I^{(j)}(t, z, \alpha) p_k(\alpha) d\alpha, \quad (2.13)$$

where

$$\mathbf{A} = \begin{pmatrix} \mathbf{A}^{(1)} & & \\ & \ddots & \\ & & \mathbf{A}^{(T)} \end{pmatrix}, \quad \mathbf{Q}(\mathbf{u}, \theta) = \begin{pmatrix} \mathbf{q}(\mathbf{u}^{(1)}, \theta) \\ \vdots \\ \mathbf{q}(\mathbf{u}^{(T)}, \theta) \end{pmatrix}, \quad \text{and} \quad \mathbf{u} = \begin{pmatrix} \mathbf{u}^{(1)} \\ \vdots \\ \mathbf{u}^{(T)} \end{pmatrix}, \quad (2.21)$$

where $\mathbf{A} \in \mathbb{R}^{(N+1)T \times (N+1)T}$, $\mathbf{Q}(\mathbf{u}, \theta) : \mathbb{R}^{(N+1)T} \times \mathbb{R}_{\geq 0} \mapsto \mathbb{R}^{(N+1)T}$, and $\mathbf{u} \in \mathbb{R}^{(N+1)T}$.

Proposition 1 Equation (2.20)–(2.21) is a system of hyperbolic partial differential equation.

Proof To prove hyperbolicity we must show that the matrix $\mathbf{A} \in \mathbb{R}^{(N+1)T \times (N+1)T}$ in (2.20)–(2.21) is diagonalizable with only real eigenvalues. Showing this is equivalent to showing that each block matrix $\mathbf{A}^{(j)} \in \mathbb{R}^{(N+1) \times (N+1)}$ is diagonalizable with only real eigenvalues, since \mathbf{A} is simply a block diagonal matrix with blocks $\mathbf{A}^{(j)}$ for $j = 1, 2, \dots, T$.

To show that $\mathbf{A}^{(j)}$ is diagonalizable with only real eigenvalues, we write the tridiagonal matrix $\mathbf{A}^{(j)}$ as follows and define a diagonal matrix \mathbf{D} :

$$\mathbf{A}^{(j)} = \begin{pmatrix} a & b_1 & & & \\ c_1 & a & b_2 & & \\ & c_2 & a & \ddots & \\ & & \ddots & \ddots & b_{N-1} \\ & & & c_{N-1} & a & b_N \\ & & & & c_N & a \end{pmatrix}, \quad \mathbf{D} = \begin{pmatrix} 1 & & & & \\ & \sqrt{\frac{c_1}{b_1}} & & & \\ & & \sqrt{\frac{c_2}{b_2}} & & \\ & & & \ddots & \\ & & & & \sqrt{\frac{c_N}{b_N}} \end{pmatrix}, \quad (2.22)$$

where $a = \mu_j$ and for all $k = 1, 2, \dots, N$: $b_k = k/(2k-1) \neq 0$ and $c_k = (k+1)/(2k+3) \neq 0$. It can then easily be shown that $\mathbf{P}^{(j)} = \mathbf{D}^{-1} \mathbf{A}^{(j)} \mathbf{D}$, where

$$\mathbf{P}^{(j)} = \begin{pmatrix} a & \sqrt{b_1 c_1} & & & \\ \sqrt{b_1 c_1} & a & \sqrt{b_2 c_2} & & \\ & \sqrt{b_2 c_2} & a & \ddots & \\ & & \ddots & \ddots & \sqrt{b_{N-1} c_{N-1}} \\ & & & \sqrt{b_{N-1} c_{N-1}} & a & \sqrt{b_N c_N} \\ & & & & \sqrt{b_N c_N} & a \end{pmatrix}. \quad (2.23)$$

Now since the matrix $\mathbf{P}^{(j)}$ is real and symmetric, it has only real eigenvalues. Also, all the eigenvalues of $\mathbf{P}^{(j)}$ are distinct since all off-diagonal elements are nonzero [27]. Hence, $\mathbf{A}^{(j)}$ has only real eigenvalues and all the eigenvalues are distinct by similarity to $\mathbf{P}^{(j)}$. \square

Proposition 2 The eigenvalues of the matrix $\mathbf{A} \in \mathbb{R}^{(N+1)T \times (N+1)T}$ in (2.20)–(2.21) are real, distinct, and given by

$$\lambda_{k+(j-1)(N-1)} = \mu_j + \left(\frac{\Delta\mu}{2} \right) s_k \quad \text{for} \quad k = 1, \dots, N+1, \quad j = 1, \dots, T, \quad (2.24)$$

where $s_k \in (-1, 1)$ for $k = 1, 2, \dots, N+1$ are the real distinct roots of the degree $(N+1)$ Legendre polynomial. If we assume that the $N+1$ Legendre roots are ordered so that s_{N+1} is the largest root (i.e., closest to $+1$), then the largest eigenvalue (in absolute value) of \mathbf{A} is given by

$$\rho(\mathbf{A}) = -\lambda_1 = \lambda_{(N+1)T} = \mu_T + \left(\frac{\Delta\mu}{2}\right) s_{N+1}. \quad (2.25)$$

Proof It can be shown that the eigenvalues of $\mathbf{A}^{(j)} \in \mathbb{R}^{(N+1) \times (N+1)}$ from (2.17) are given by the following formula (e.g., see Cohen [5]):

$$\lambda_k^{(j)} = \mu_j + \left(\frac{\Delta\mu}{2}\right) s_k, \quad \text{for } k = 1, 2, \dots, N+1, \quad (2.26)$$

where $s_k \in (-1, 1)$ for $k = 1, 2, \dots, N+1$ are the roots of the degree $(N+1)$ Legendre polynomial. Since \mathbf{A} is just a block diagonal matrix with $\mathbf{A}^{(j)} \in \mathbb{R}^{(N+1) \times (N+1)}$ as the blocks for $j = 1, 2, \dots, T$ (as shown in (2.21)), it follows that the eigenvalues of \mathbf{A} are of the form:

$$\lambda_{k+(j-1)(N+1)} = \mu_j + \left(\frac{\Delta\mu}{2}\right) s_k \quad \text{for } k = 1, \dots, N+1, \quad j = 1, \dots, T. \quad (2.27)$$

The most negative and most positive eigenvalues in (2.27) are λ_1 ($k = 1, j = 1$) and $\lambda_{(N+1)T}$ ($k = N+1, j = T$), respectively. This follows directly from the assumed ordering of s_k , as well as the ordering assumed in the definition of μ_j (see equation (2.9)). In fact, these two eigenvalues have the same magnitude, since by definition: $s_1 = -s_{N+1}$ and $\mu_1 = -\mu_T$. This gives the desired result: equation (2.25).

Proposition 3 $\rho(\mathbf{A}) < 1$ for any T and N of H_N^T .

Proof A simple calculation, using the fact that $s_{N+1} < 1$, shows that

$$\begin{aligned} \rho(\mathbf{A}) &= \mu_T + \left(\frac{\Delta\mu}{2}\right) s_{N+1} = 1 - \left(\frac{\Delta\mu}{2}\right) + \left(\frac{\Delta\mu}{2}\right) s_{N+1} < 1 - \left(\frac{\Delta\mu}{2}\right) + \left(\frac{\Delta\mu}{2}\right) = 1, \\ &\implies \rho(\mathbf{A}) < 1. \end{aligned}$$

Furthermore, we note that $\rho(\mathbf{A}) = 1 - \mathcal{O}(\Delta\mu)$ as $\Delta\mu \rightarrow 0$. □

Remark 2.1 We have shown via the above propositions that all of the eigenvalues of \mathbf{A} are real, distinct, and strictly between -1 and 1 . In practice, we would also like to impose the condition that \mathbf{A} not have a zero eigenvalue; this additional requirement is useful especially in the computation of steady-state solutions and in the imposition of inflow/outflow boundary conditions. We can always ensure that \mathbf{A} does not have a zero eigenvalue if either of the following conditions are satisfied:

1. T is even; or
2. T is odd and N is odd.

These assertions follow directly from definition (2.27).

2.3 The radiation energy density

Using the H_N^T ansatz (2.10), the angular moment of the radiation density (2.5) can be written as follows:

$$\begin{aligned} E(t, z) &:= \frac{1}{c} \int_{-1}^1 I(t, z, \mu) d\mu = \frac{1}{c} \frac{\Delta\mu}{2} \sum_{j=1}^T \int_{-1}^1 I^{(j)}(t, z, \alpha) d\alpha \\ &= \frac{\Delta\mu}{2c} \sum_{j=1}^T \int_{-1}^1 \sum_{k=0}^N \left(\frac{2k+1}{2} \right) u_k^{(j)}(t, z) p_k(\alpha) d\alpha = \frac{\Delta\mu}{2c} \sum_{j=1}^T u_0^{(j)}(t, z). \end{aligned} \quad (2.28)$$

Using this result, we can rewrite material-energy equation (2.8) as follows:

$$C_v \frac{\partial \theta}{\partial t} = \frac{\sigma \Delta\mu}{2} \sum_{j=1}^T u_0^{(j)}(t, z) - \sigma a c \theta^4. \quad (2.29)$$

3 Semi-implicit discontinuous Galerkin (DG) method

In this section we develop a discontinuous Galerkin (DG) finite element method with a semi-implicit time discretization for solving the 1D H_N^T system (2.20)–(2.21) along with the material-energy equation (2.29). The strategy that we employ is similar to the method developed by McClarren et al. [21] for the P_N equations, but here we extend that work to the H_N^T approximation as described above.

3.1 Discontinuous Galerkin spatial discretization

The H_N^T approximation as described in the previous sections divides the phase space into discrete velocity bands, inside of which we approximate the specific intensity, $I(t, x, \mu)$, by a finite polynomial ansatz; this is illustrated in Figure Figure 2.1(a). In order to spatially discretize the resulting H_N^T equations: (2.20)–(2.21) and (2.29), we additionally introduce a mesh in the z -coordinate:

$$[z_L, z_R] = \bigcup_{i=1}^{N_z} \mathcal{T}_i, \quad \text{where} \quad \mathcal{T}_i = \left[z_i - \frac{\Delta z}{2}, z_i + \frac{\Delta z}{2} \right], \quad (3.1)$$

$$z_i = z_L + \left(i - \frac{1}{2} \right) \Delta z, \quad \text{and} \quad \Delta z = \frac{z_R - z_L}{N_z}. \quad (3.2)$$

The full $z - \mu$ phase space mesh is illustrated in Figure Figure 2.1(b). On each mesh element we define a local coordinate as follows:

$$z \Big|_{\mathcal{T}_i} = z_i + \left(\frac{\Delta z}{2} \right) \xi, \quad \text{where} \quad \xi \in [-1, 1]. \quad (3.3)$$

The test and trial functions for the discontinuous Galerkin scheme will come from following *broken* finite element spaces:

$$\mathcal{W}_{M_{\text{eqn}}}^{\Delta z} := \left\{ \mathbf{w}^{\Delta z} \in \left[L^\infty [z_L, z_R] \right]^{M_{\text{eqn}}} : \mathbf{w}^{\Delta z} \Big|_{\mathcal{T}_i} \in \left[\mathbb{P}(M_{\text{deg}}) \right]^{M_{\text{eqn}}} \forall \mathcal{T}_i \right\}, \quad (3.4)$$

where M_{eqn} is the number of equations and $\mathbb{P}(M_{\text{deg}})$ is the set of all polynomials with maximum polynomial order M_{deg} . On each mesh element we define the $M_{\text{deg}} + 1$ Gauss-Lobatto points: $\xi_j \in [-1, 1]$ for $j = 1, \dots, M_{\text{deg}} + 1$ (e.g., see [35]). For each Gauss-Lobatto point we define the associated Lagrange interpolating polynomial:

$$\Phi_j(\xi) = \prod_{\substack{k=1 \\ k \neq j}}^{M_{\text{deg}}+1} \frac{(\xi - \xi_k)}{(\xi_j - \xi_k)}, \quad \text{s.t.} \quad \Phi_j(\xi_\ell) = \delta_{j\ell} \quad \text{for} \quad j, \ell = 1, \dots, M_{\text{deg}} + 1. \quad (3.5)$$

The approximate solution on each element can then be written as

$$\left\{ \mathbf{u}^{\Delta z}(t, z(\xi)), \theta^{\Delta z}(t, z(\xi)) \right\} \Big|_{\mathcal{T}_i} = \sum_{j=1}^{M_{\text{deg}}+1} \left\{ \mathbf{U}_{ij}(t), \Theta_{ij}(t) \right\} \Phi_j(\xi), \quad (3.6)$$

where $\mathbf{u}^{\Delta z}(t, z) : \mathbb{R}_{\geq 0} \times \mathbb{R} \mapsto \mathcal{W}_{(N+1)T}^{\Delta z}$, $\theta^{\Delta z}(t, z) : \mathbb{R}_{\geq 0} \times \mathbb{R} \mapsto \mathcal{W}_1^{\Delta z}$, $\Phi_j(\xi) : [-1, 1] \mapsto \mathbb{R}$, and $\mathbf{U}_j(t) : \mathbb{R}_{\geq 0} \mapsto \mathbb{R}^{(N+1)T}$. Similarly, we write the approximate source as

$$\mathbf{Q}^{\Delta z}(\mathbf{u}^{\Delta z}, \theta^{\Delta z}) \Big|_{\mathcal{T}_i} = \sum_{j=1}^{M_{\text{deg}}+1} \mathbf{Q}(\mathbf{U}_{ij}(t), \Theta_{ij}(t)) \Phi_j(\xi). \quad (3.7)$$

To obtain the spatially discretized version of \mathbf{H}_N^T system (2.20) on each element \mathcal{T}_i , we replace the exact solution by (3.6), the exact source by (3.7), multiply (2.20) by a test function $\Phi_k(\xi)$, integrate over the element, and apply integration-by-parts in ξ :

$$\begin{aligned} \frac{1}{c} \sum_{j=1}^{M_{\text{deg}}+1} \frac{d\mathbf{U}_{ij}(t)}{dt} M_{kj} + \left(\frac{2}{\Delta z} \right) \left[\Phi_k(1) \mathcal{F}_{i+\frac{1}{2}}(t) - \Phi_k(-1) \mathcal{F}_{i-\frac{1}{2}}(t) \right] \\ - \left(\frac{2}{\Delta z} \right) \mathbf{A} \sum_{j=1}^{M_{\text{deg}}+1} \mathbf{U}_{ij}(t) N_{kj} = \sum_{j=1}^{M_{\text{deg}}+1} \mathbf{Q}(\mathbf{U}_{ij}(t), \Theta_{ij}(t)) M_{kj}, \end{aligned} \quad (3.8)$$

for each $k = 1, \dots, M_{\text{deg}}$, where we used the fact that $\partial_z = (2/\Delta z) \partial_\xi$, and where

$$M_{kj} = \int_{-1}^1 \Phi_k(\xi) \Phi_j(\xi) d\xi \quad \text{and} \quad N_{kj} = \int_{-1}^1 \Phi_j(\xi) \Phi'_k(\xi) d\xi. \quad (3.9)$$

The numerical flux on each element face is defined as follows:

$$\begin{aligned} \mathcal{F}_{i-\frac{1}{2}}(t) = \frac{1}{2} \mathbf{A} \sum_{j=1}^{M_{\text{deg}}+1} \left(\mathbf{U}_{i-1j}(t) \Phi_j(1) + \mathbf{U}_{ij}(t) \Phi_j(-1) \right) \\ + \frac{1}{2} |\mathbf{A}| \sum_{j=1}^{M_{\text{deg}}+1} \left(\mathbf{U}_{i-1j}(t) \Phi_j(1) - \mathbf{U}_{ij}(t) \Phi_j(-1) \right), \end{aligned} \quad (3.10)$$

for $i = 1, \dots, N_z + 1$. In the above expression, $|\mathbf{A}|$ is defined through the eigenvalues of \mathbf{A} :

$$\mathbf{A} = \mathbf{V}\mathbf{\Lambda}\mathbf{V}^{-1} \implies |\mathbf{A}| = \mathbf{V}|\mathbf{\Lambda}|\mathbf{V}^{-1}, \quad (3.11)$$

where \mathbf{V} is the matrix of right eigenvectors of \mathbf{A} , $\mathbf{\Lambda} = \text{diag}(\lambda_1, \dots, \lambda_{(N+1)T})$ is the diagonal matrix of eigenvalues of \mathbf{A} , and $|\mathbf{\Lambda}| = \text{diag}(|\lambda_1|, \dots, |\lambda_{(N+1)T}|)$.

In order to close this semi-discrete system, we also need to semi-discretize material-energy equation (2.29). Following all of the above outlined procedures, this results in the following equation:

$$C_v \sum_{j=1}^{M_{\text{deg}}+1} \frac{d\Theta_{ij}(t)}{dt} M_{kj} = \sum_{j=1}^{M_{\text{deg}}+1} \left(\frac{\sigma\Delta\mu}{2} \sum_{\ell=1}^T U_{ij(1)}^{(\ell)}(t) - \sigma ac (\Theta_{ij}(t))^4 \right) M_{kj}, \quad (3.12)$$

where $U_{ij(1)}^{(\ell)}$ refers to the $(1 + (\ell - 1)(N + 1))^{\text{th}}$ component of \mathbf{U}_{ij} (i.e., the first component of \mathbf{U}_{ij} in the ℓ^{th} velocity band).

For the remainder of this paper we consider the case $M_{\text{deg}} = 1$ (i.e., the piecewise linear DG approximation), which yields a second-order accurate spatial approximation. The basis functions in this case are

$$\Phi_1(\xi) = \frac{1}{2}(1 - \xi) \quad \text{and} \quad \Phi_2(\xi) = \frac{1}{2}(1 + \xi). \quad (3.13)$$

In this case, all of the above expressions simplify greatly. For example, the values defined in (3.8) reduce to the following:

$$\mathbf{M} = \frac{1}{3} \begin{bmatrix} 2 & 1 \\ 1 & 2 \end{bmatrix} \quad \text{and} \quad \mathbf{N} = \frac{1}{2} \begin{bmatrix} -1 & -1 \\ 1 & 1 \end{bmatrix}. \quad (3.14)$$

After some simple algebra, we arrive at the following semi-discrete system:

$$\frac{1}{c} \frac{d\mathbf{U}_{i1}}{dt} - \frac{2\mathcal{F}_{i+\frac{1}{2}} + 4\mathcal{F}_{i-\frac{1}{2}} - 3\mathbf{A}(\mathbf{U}_{i1} + \mathbf{U}_{i2})}{\Delta z} = \mathbf{Q}(\mathbf{U}_{i1}, \Theta_{i1}), \quad (3.15)$$

$$\frac{1}{c} \frac{d\mathbf{U}_{i2}}{dt} + \frac{4\mathcal{F}_{i+\frac{1}{2}} + 2\mathcal{F}_{i-\frac{1}{2}} - 3\mathbf{A}(\mathbf{U}_{i1} + \mathbf{U}_{i2})}{\Delta z} = \mathbf{Q}(\mathbf{U}_{i2}, \Theta_{i2}), \quad (3.16)$$

$$C_v \frac{d\Theta_{ij}}{dt} = \frac{\sigma\Delta\mu}{2} \sum_{\ell=1}^T U_{ij(1)}^{(\ell)} - \sigma ac \Theta_{ij}^4, \quad \text{for } j = 1, 2, \quad (3.17)$$

for $i = 1, \dots, (N + 1)T$. The numerical fluxes in the $M_{\text{deg}} = 1$ reduces to the following:

$$\mathcal{F}_{i-\frac{1}{2}}(t) = \frac{1}{2}\mathbf{A}(\mathbf{U}_{i1}(t) + \mathbf{U}_{i-12}(t)) - \frac{1}{2}|\mathbf{A}|(\mathbf{U}_{i1}(t) - \mathbf{U}_{i-12}(t)), \quad (3.18)$$

for $i = 1, \dots, N_z + 1$.

3.2 Semi-implicit time scheme: nonlinear version

For the time integration we adopt the semi-implicit scheme by McClarren et al. [21], which is a two-stage Runge-Kutta method. The first stage (i.e., the predictor step) can be written as follows:

$$\frac{1}{c} \frac{\mathbf{U}_{i1}^{n+\frac{1}{2}} - \mathbf{U}_{i1}^n}{\Delta t/2} = + \frac{2\mathcal{F}_{i+\frac{1}{2}}^n + 4\mathcal{F}_{i-\frac{1}{2}}^n - 3\mathbf{A}(\mathbf{U}_{i1}^n + \mathbf{U}_{i2}^n)}{\Delta z} + \mathbf{Q}(\mathbf{U}_{i1}^{n+\frac{1}{2}}, \Theta_{i1}^{n+\frac{1}{2}}), \quad (3.19)$$

$$\frac{1}{c} \frac{\mathbf{U}_{i2}^{n+\frac{1}{2}} - \mathbf{U}_{i2}^n}{\Delta t/2} = - \frac{4\mathcal{F}_{i+\frac{1}{2}}^n + 2\mathcal{F}_{i-\frac{1}{2}}^n - 3\mathbf{A}(\mathbf{U}_{i1}^n + \mathbf{U}_{i2}^n)}{\Delta z} + \mathbf{Q}(\mathbf{U}_{i2}^{n+\frac{1}{2}}, \Theta_{i2}^{n+\frac{1}{2}}), \quad (3.20)$$

$$C_v \frac{\Theta_{ij}^{n+\frac{1}{2}} - \Theta_{ij}^n}{\Delta t/2} = \frac{\sigma \Delta \mu}{2} \sum_{\ell=1}^T U_{ij(\ell)}^{(\ell)n+\frac{1}{2}} - \sigma ac \left(\Theta_{ij}^{n+\frac{1}{2}} \right)^4, \quad \text{for } j = 1, 2. \quad (3.21)$$

Similarly, the second stage (i.e., the correction step) can be written as follows:

$$\frac{1}{c} \frac{\mathbf{U}_{i1}^{n+1} - \mathbf{U}_{i1}^n}{\Delta t} = + \frac{2\mathcal{F}_{i+\frac{1}{2}}^{n+\frac{1}{2}} + 4\mathcal{F}_{i-\frac{1}{2}}^{n+\frac{1}{2}} - 3\mathbf{A}(\mathbf{U}_{i1}^{n+\frac{1}{2}} + \mathbf{U}_{i2}^{n+\frac{1}{2}})}{\Delta z} + \mathbf{Q}(\mathbf{U}_{i1}^{n+1}, \Theta_{i1}^{n+1}), \quad (3.22)$$

$$\frac{1}{c} \frac{\mathbf{U}_{i2}^{n+1} - \mathbf{U}_{i2}^n}{\Delta t} = - \frac{4\mathcal{F}_{i+\frac{1}{2}}^{n+\frac{1}{2}} + 2\mathcal{F}_{i-\frac{1}{2}}^{n+\frac{1}{2}} - 3\mathbf{A}(\mathbf{U}_{i1}^{n+\frac{1}{2}} + \mathbf{U}_{i2}^{n+\frac{1}{2}})}{\Delta z} + \mathbf{Q}(\mathbf{U}_{i2}^{n+1}, \Theta_{i2}^{n+1}), \quad (3.23)$$

$$C_v \frac{\Theta_{ij}^{n+1} - \Theta_{ij}^n}{\Delta t} = \frac{\sigma \Delta \mu}{2} \sum_{\ell=1}^T U_{ij(\ell)}^{(\ell)n+1} - \sigma ac \left(\Theta_{ij}^{n+1} \right)^4, \quad \text{for } j = 1, 2. \quad (3.24)$$

The numerical flux in both the first and second stages is of the following form:

$$\mathcal{F}_{i-\frac{1}{2}}^\star = \frac{1}{2} \mathbf{A}(\mathbf{U}_{i1}^\star + \mathbf{U}_{i-12}^\star) - \frac{1}{2} |\mathbf{A}| (\mathbf{U}_{i1}^\star - \mathbf{U}_{i-12}^\star), \quad (3.25)$$

where $\star \in \{n, n + \frac{1}{2}\}$.

The time-stepping scheme described above is semi-implicit in that it is explicit on the wave propagation terms and implicit on the collision terms. Since in the TRT system the collision source is a nonlinear function of the temperature, the result is that in each stage a nonlinear algebraic equation must be solved. In order to avoid this, we show in the next section how to linearize the source.

3.3 Semi-implicit time scheme: linearized version

The scheme we propose in this work for solving the 1D \mathbf{H}_N^T system (2.20)–(2.21) along with the material-energy equation (2.29) is a variant of the semi-implicit scheme described by (3.19)–(3.24), but with the additional feature that the source is linearized. The proposed scheme is a \mathbf{H}_N^T extension of the scheme developed for the \mathbf{P}_N system in [21]. The details of this scheme are provided in this section.

We begin this discussion by recalling that source, \mathbf{Q} , in (3.19)–(3.20) and (3.22)–(3.23) can be written as follows:

$$\mathbf{Q}\left(\mathbf{U}_{ij}^{\star}, \Theta_{ij}^{\star}\right) = -\sigma \mathbf{U}_{ij}^{\star} + \sigma ac \left(\Theta_{ij}^{\star}\right)^4 \tilde{\mathbf{e}}, \quad (3.26)$$

where $\star \in \left\{n + \frac{1}{2}, n + 1\right\}$ and $\tilde{\mathbf{e}} \in \mathbb{R}^{(N+1)T}$ is a vector with the following components:

$$\tilde{e}_m = \begin{cases} 1 & \text{if } m = 1 + (k-1)(N+1) \text{ for } k = 1, 2, \dots, T, \\ 0 & \text{otherwise.} \end{cases} \quad (3.27)$$

These sources are clearly nonlinear in the temperature Θ . In order to linearize \mathbf{Q} we invoke the following two Taylor expansions in temperature:

$$\left(\Theta_{ij}^{n+\frac{1}{2}}\right)^4 = \left(\Theta_{ij}^n\right)^4 + 4\left(\Theta_{ij}^n\right)^3 \left(\Theta_{ij}^{n+\frac{1}{2}} - \Theta_{ij}^n\right) + \mathcal{O}\left(\left(\Theta_{ij}^{n+\frac{1}{2}} - \Theta_{ij}^n\right)^2\right), \quad (3.28)$$

$$\left(\Theta_{ij}^{n+1}\right)^4 = \left(\Theta_{ij}^n\right)^4 + 4\left(\Theta_{ij}^n\right)^3 \left(\Theta_{ij}^{n+1} - \Theta_{ij}^n\right) + \mathcal{O}\left(\left(\Theta_{ij}^{n+1} - \Theta_{ij}^n\right)^2\right). \quad (3.29)$$

Since our overall method is only accurate to second order, we can safely disregard the second order corrections in the above expressions. Furthermore, the linear differences in the Taylor expansions can be replaced via the update formulas (3.21) and (3.24), respectively, yielding:

$$\left(\Theta_{ij}^{n+\frac{1}{2}}\right)^4 \approx \left(\Theta_{ij}^n\right)^4 + 4\left(\Theta_{ij}^n\right)^3 \frac{\Delta t}{2C_v} \left(\frac{\sigma \Delta \mu}{2} \sum_{\ell=1}^T U_{ij(1)}^{(\ell)n+\frac{1}{2}} - \sigma ac \left(\Theta_{ij}^{n+\frac{1}{2}}\right)^4\right), \quad (3.30)$$

$$\left(\Theta_{ij}^{n+1}\right)^4 \approx \left(\Theta_{ij}^n\right)^4 + 4\left(\Theta_{ij}^n\right)^3 \frac{\Delta t}{C_v} \left(\frac{\sigma \Delta \mu}{2} \sum_{\ell=1}^T U_{ij(1)}^{(\ell)n+1} - \sigma ac \left(\Theta_{ij}^{n+1}\right)^4\right). \quad (3.31)$$

Treating the above approximations as equalities and solving (3.30) and (3.31) for the fourth power of $\Theta_{ij}^{n+\frac{1}{2}}$ and Θ_{ij}^{n+1} , respectively, yields:

$$\left(\tilde{\Theta}_{ij}^{n+\frac{1}{2}}\right)^4 := \frac{\left(\Theta_{ij}^n\right)^3 \left(C_v \Theta_{ij}^n + \Delta t \Delta \mu \sigma \sum_{\ell=1}^T U_{ij(1)}^{(\ell)n+\frac{1}{2}}\right)}{C_v + 2\Delta t ac \sigma \left(\Theta_{ij}^n\right)^3}, \quad (3.32)$$

$$\left(\tilde{\Theta}_{ij}^{n+1}\right)^4 := \frac{\left(\Theta_{ij}^n\right)^3 \left(C_v \Theta_{ij}^n + 2\Delta t \Delta \mu \sigma \sum_{\ell=1}^T U_{ij(1)}^{(\ell)n+1}\right)}{C_v + 4\Delta t ac \sigma \left(\Theta_{ij}^n\right)^3}. \quad (3.33)$$

Using these versions of the fourth power of the temperature successfully linearizes the source terms in (3.19)–(3.20) and (3.22)–(3.23).

In order to complete the linearization of the source terms, we now turn our attention to (3.24). In particular, we replace the fourth power of Θ_{ij}^{n+1} in (3.24) by (3.33). After

some simple algebra, we now arrive at the final semi-implicit discontinuous Galerkin scheme that is advocated in this work. The first stage is

$$\frac{1}{c} \frac{\mathbf{U}_{i1}^{n+\frac{1}{2}} - \mathbf{U}_{i1}^n}{\Delta t/2} = + \frac{2\mathcal{F}_{i+\frac{1}{2}}^n + 4\mathcal{F}_{i-\frac{1}{2}}^n - 3\mathbf{A}(\mathbf{U}_{i1}^n + \mathbf{U}_{i2}^n)}{\Delta z} - \sigma \mathbf{U}_{i1}^{n+\frac{1}{2}} + \sigma ac \left(\tilde{\Theta}_{i1}^{n+\frac{1}{2}} \right)^4 \tilde{\mathbf{e}}, \quad (3.34)$$

$$\frac{1}{c} \frac{\mathbf{U}_{i2}^{n+\frac{1}{2}} - \mathbf{U}_{i2}^n}{\Delta t/2} = - \frac{4\mathcal{F}_{i+\frac{1}{2}}^n + 2\mathcal{F}_{i-\frac{1}{2}}^n - 3\mathbf{A}(\mathbf{U}_{i1}^n + \mathbf{U}_{i2}^n)}{\Delta z} - \sigma \mathbf{U}_{i2}^{n+\frac{1}{2}} + \sigma ac \left(\tilde{\Theta}_{i2}^{n+\frac{1}{2}} \right)^4 \tilde{\mathbf{e}}, \quad (3.35)$$

where $\tilde{\Theta}$ is defined by (3.32) and $\tilde{\mathbf{e}}$ is defined by (3.27). The second stage is

$$\frac{1}{c} \frac{\mathbf{U}_{i1}^{n+1} - \mathbf{U}_{i1}^n}{\Delta t} = + \frac{2\mathcal{F}_{i+\frac{1}{2}}^{n+\frac{1}{2}} + 4\mathcal{F}_{i-\frac{1}{2}}^{n+\frac{1}{2}} - 3\mathbf{A}(\mathbf{U}_{i1}^{n+\frac{1}{2}} + \mathbf{U}_{i2}^{n+\frac{1}{2}})}{\Delta z} - \sigma \mathbf{U}_{i1}^{n+1} + \sigma ac \left(\tilde{\Theta}_{i1}^{n+1} \right)^4 \tilde{\mathbf{e}}, \quad (3.36)$$

$$\frac{1}{c} \frac{\mathbf{U}_{i2}^{n+1} - \mathbf{U}_{i2}^n}{\Delta t} = - \frac{4\mathcal{F}_{i+\frac{1}{2}}^{n+\frac{1}{2}} + 2\mathcal{F}_{i-\frac{1}{2}}^{n+\frac{1}{2}} - 3\mathbf{A}(\mathbf{U}_{i1}^{n+\frac{1}{2}} + \mathbf{U}_{i2}^{n+\frac{1}{2}})}{\Delta z} - \sigma \mathbf{U}_{i2}^{n+1} + \sigma ac \left(\tilde{\Theta}_{i2}^{n+1} \right)^4 \tilde{\mathbf{e}}, \quad (3.37)$$

$$\Theta_{ij}^{n+1} = \Theta_{ij}^n + \frac{\sigma \Delta t \left[\frac{\Delta \mu}{2} \sum_{\ell=1}^T U_{ij(1)}^{(\ell)n+1} - ac \left(\Theta_{ij}^n \right)^4 \right]}{C_v + 4\Delta t ac \sigma \left(\Theta_{ij}^n \right)^3}, \quad \text{for } j = 1, 2, \quad (3.38)$$

where $\tilde{\Theta}$ is defined by (3.33) and $\tilde{\mathbf{e}}$ is defined by (3.27). Note that by the time we reach (3.38), \mathbf{U}_{ij}^{n+1} is already known, meaning that this step has the computational complexity of an explicit update. Again, the numerical fluxes in both the first and second stages are of the form (3.25).

3.4 Slope limiter

In order to remove unphysical oscillations from the numerical method described above, we include a slope limiter. McClarren and Lowrie [23] pointed out that the *double minmod* slope limiter, also known as the *monotonized central* slope limiter, is asymptotic-preserving for hyperbolic systems with stiff relaxation terms while the minmod limiter does not preserve the asymptotic limit due to discontinuities at the cell edge. Therefore, in this work we use the same double minmod limiter to preserve asymptotic limit. In particular, after each predictor and corrector step we compute the cell average:

$$\bar{\mathbf{U}}_i = \frac{\mathbf{U}_{i1} + \mathbf{U}_{i2}}{2}, \quad (3.39)$$

and then modify the original nodal values as

$$\mathbf{U}_{i1} := \bar{\mathbf{U}}_i - \frac{\mathbf{S}_i}{2} \quad \text{and} \quad \mathbf{U}_{i2} := \bar{\mathbf{U}}_i + \frac{\mathbf{S}_i}{2}, \quad (3.40)$$

where

$$s_{i(\ell)} = \text{mm}\left(U_{i2(\ell)} - U_{i1(\ell)}, \alpha \left(\bar{U}_{i(\ell)} - \bar{U}_{i-1(\ell)}\right), \alpha \left(\bar{U}_{i+1(\ell)} - \bar{U}_{i(\ell)}\right)\right), \quad (3.41)$$

where $\alpha \in [0, 2]$, $i = 1, \dots, N_z$, $l = 1, \dots, T(N+1)$, and the minmod function is defined as follows:

$$\text{mm}(a, b, c) := \begin{cases} \text{sign}(a) \min(|a|, |b|, |c|), & \text{if } \text{sign}(a) = \text{sign}(b) = \text{sign}(c), \\ 0, & \text{otherwise.} \end{cases} \quad (3.42)$$

As explained in [21], $\alpha = 0$ is the first-order upwind or Godunov scheme, $\alpha = 1$ is the minmod limiter, and $\alpha = 2$ is the monotized central (MC) or double minmod limiter. We use $\alpha = 2$ in all our numerical tests.

3.5 Boundary conditions

To complete the numerical methods section, we briefly explain how boundary conditions are implemented. The three types of boundary conditions considered in this work in various examples are reflective, Dirichlet, and vacuum conditions. In all cases we prescribe the intensities on the left and right boundaries via the following expressions:

$$I^L(t, \mu) = \begin{cases} I_{\text{out}}(t, z_L, \mu) & \text{if } \mu > 0, \\ I(t, z_L, \mu) & \text{if } \mu < 0, \end{cases} \quad I^R(t, \mu) = \begin{cases} I(t, z_R, \mu) & \text{if } \mu > 0, \\ I_{\text{out}}(t, z_R, \mu) & \text{if } \mu < 0, \end{cases} \quad (3.43)$$

respectively, where

$$I_{\text{out}}(t, z, \mu) = \begin{cases} I(t, z, -\mu) & \text{if reflective BC,} \\ I(t, z, \mu) & \text{if Dirichlet BC,} \\ 0 & \text{if vacuum BC.} \end{cases} \quad (3.44)$$

Note that z_L and z_R denote the left and right boundaries, respectively.

4 Numerical results

In this section, numerical results for six standard benchmark problems for the TRT system are provided, including examples in the optically thin and thick regimes: (1) bilateral inflow (§4.1), (2) streaming in a vacuum (§4.2), (3) Su-Olson problem (§4.3), (4) diffusive Marshak wave (§4.4), (5) Marshak wave in thin medium (§4.5), and (6) smooth Marshak wave problem (§4.6). The material-energy coupling equation (2.29) is only required for in the examples described in §4.3–§4.6.

Unless otherwise stated, we choose a CFL condition for all simulations as follows:

$$\text{CFL} := \frac{c \rho(\mathbf{A}) \Delta t}{\Delta x} \leq 0.3, \quad (4.1)$$

where $\rho(\mathbf{A}) \approx 1$ is the spectral radius of a matrix \mathbf{A} as defined in equation (2.25). For numerical examples in which the diffusion dominates, for example problems like the diffusive Marshak wave problem, we are able to achieve very relaxed CFL number between 2 and 3.

4.1 Bilateral inflow

This problem is used to test the H_N^T scheme without the opacity σ and the external source s ; this shows how well the hybrid discrete approximation of the free-streaming kinetic operator and its corresponding numerical discretization captures the correct wave speeds and resolves discontinuities. In this setting, equation (2.7) reduces to the following:

$$\frac{1}{c} \frac{\partial I}{\partial t} + \mu \frac{\partial I}{\partial z} = 0, \quad (4.2)$$

for which the analytic solution can easily be computed from the method of characteristics (e.g., see [7]):

$$I(t, z, \mu) = I^0(z - c\mu t, \mu). \quad (4.3)$$

We choose the initial condition as

$$I^0(z, \mu) = \begin{cases} ac\delta(\mu - 1) & \text{if } z \leq 0.2, \\ 0 & \text{if } 0.2 < z < 0.8, \\ 0.5ac & \text{if } z > 0.8, \end{cases} \quad (4.4)$$

where $\delta(\mu - 1)$ is a Dirac delta centered at $\mu = 1$, $c = 3 \times 10^{10} \text{ cm s}^{-1}$ is the speed of light, and $a = 1.372 \times 10^{14} \text{ ergs cm}^{-3} \text{ keV}^{-4}$ is the radiation constant. The exact angular moment of the radiation intensity, $E(t, z)$, is given by the following if $0 < ct < 0.3$:

$$a^{-1}E(t, z) = \begin{cases} 1 & \text{if } z \leq 0.2 + ct, \\ 0 & \text{if } 0.2 + ct < z \leq 0.8 - ct, \\ (z - 0.8 + ct)/(2ct) & \text{if } 0.8 - ct \leq z \leq 0.8 + ct, \\ 1 & \text{if } z \geq 0.8 + ct. \end{cases} \quad (4.5)$$

We run the code until $ct_{\text{end}} = 0.1$, in the physical domain $z \in [0, 1]$ with inflow/outflow boundary conditions based on the exact solution (4.3)–(4.4). This example is challenging for moment closure methods such as P_N and H_N^T due to the fact that there is a delta function in velocity, as well as discontinuities in both z and μ . Furthermore, in this example there are no collisions to help smooth out the solution.

The scaled angular moment of the radiation intensity, $E(t, z)/a$, for various P_N and H_N^T approximations are shown in Figure 4.1. Each panel in Figure 4.1 shows solutions with models that have the same DOFs: (a) 4 moments: P_3 and H_1^2 , (b) 6

moments: P_5 , H_1^3 , and H_2^2 , (c) 8 moments: P_7 , H_1^4 , and H_3^2 , and (d) 24 moments: P_{23} , H_1^{12} , and H_5^4 . In each case, the H_N^T model with $T > 1$ gives less oscillation than the P_N model with the same DOFs.

In all the simulations shown in Figure 4.1 we have used the double minmod limiter to control unphysical oscillations and to remove negative density values; without the double minmod limiters active, both P_N and H_N^T solutions suffer from negative densities near the discontinuity. In order to show how the double minmod limiter affects the solution we also provide Figure 4.2, in which we show a direct comparison of the unlimited and limited H_3^4 solutions.

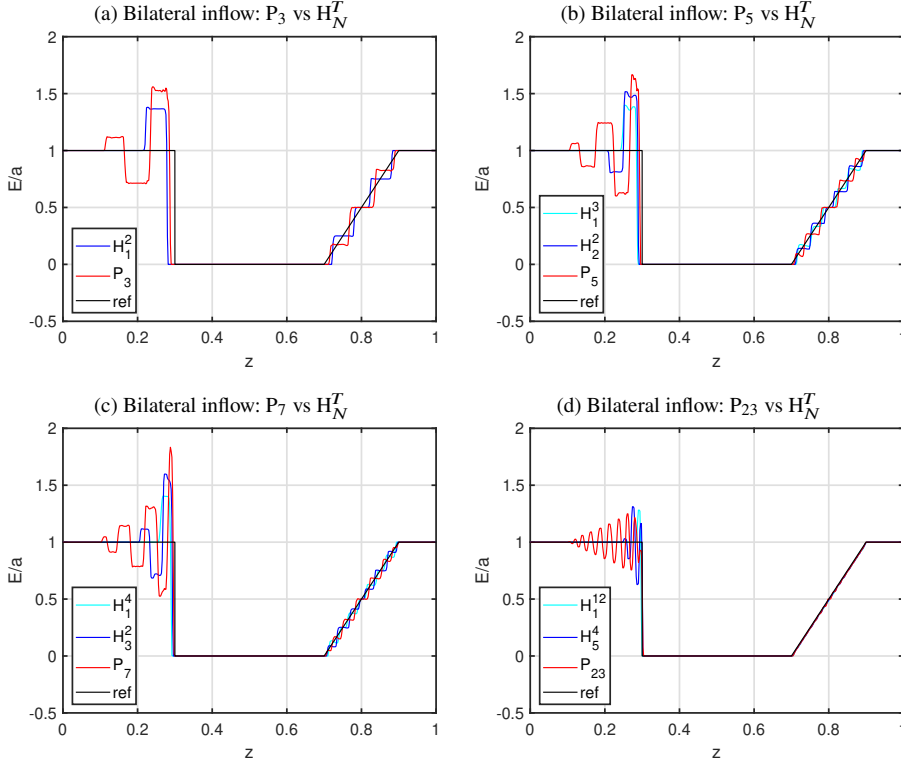


Fig. 4.1: (§4.1: Bilateral inflow) Comparisons of P_N and H_N^T solutions for the bilateral inflow problem at $ct = 0.1$, $N_z = 500$, with $CFL = 0.3$.

4.2 Streaming in a vacuum

In this section, we test our scheme on the propagation of photons in a vacuum. We choose a zero initial condition, $I^0(z, \mu) = 0$, on the computational domain $z \in [0, 1]$

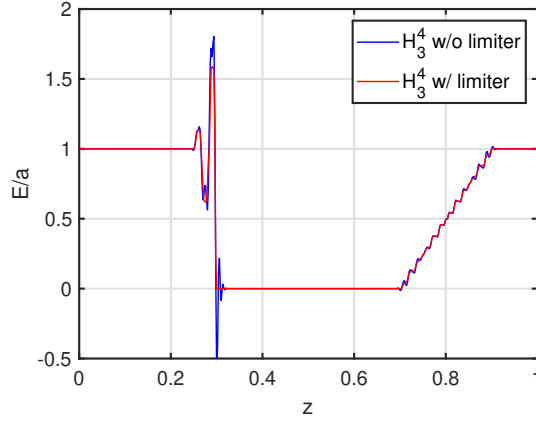


Fig. 4.2: (§4.1: Bilateral inflow) H_3^4 solution with and without the double minmod limiter for the bilateral inflow problem at $ct = 0.1$, $N_z = 500$, with CFL = 0.1.

with the following Dirichlet boundary conditions:

$$I(t, z = 0, \mu) = ac \quad \text{and} \quad I(t, z = 1, \mu) = 0. \quad (4.6)$$

The analytic solution for $t > 0$ with the given initial and boundary conditions can be obtained by the method of characteristics as in the previous bilateral problem:

$$I(t, z, \mu) = \begin{cases} ac & \text{if } z/(ct) < \mu \leq 1, \\ 0 & \text{if } -1 \leq \mu \leq z/(ct). \end{cases} \quad (4.7)$$

The exact solution for the angular momentum for $t > 0$ in this case is

$$a^{-1}E(t, z) = \int_{z/(ct)}^1 d\mu = 1 - z/(ct). \quad (4.8)$$

In Figure 4.3 and Table 4.1 we compute the absolute L_2 error in the scaled angular moments, $E(t, z)/a$, for various H_N^T approximations:

$$L_2 \text{ error} := \left[\frac{1}{aN_z} \sum_{i=1}^{N_z} \left(E_N^T(t_{\text{end}}, z_i) - E_{\text{exact}}(t_{\text{end}}, z_i) \right)^2 \right]^{1/2}, \quad (4.9)$$

$$L_\infty \text{ error} := \max_{1 \leq i \leq N_z} \left| \frac{1}{a} \left(E_N^T(t_{\text{end}}, z_i) - E_{\text{exact}}(t_{\text{end}}, z_i) \right) \right|, \quad (4.10)$$

where E_N^T is the angular momentum solution calculated using the H_N^T approximation. In particular, we show in Figure 4.3a the L_2 convergence of H_N^T with increasing N and in Figure 4.3b the L_2 convergence of H_N^T with increasing T . Figure 4.3a shows rapid convergence in terms of N for the H_N^2 and H_N^3 solutions, however $P_N = (H_N^1)$ shows a much slower convergence rate. Meanwhile, Figure 4.3b shows rapid convergence with a much steeper slope than Figure 4.3a, which suggests that increasing T is a better

way to achieve the desired accuracy than increasing N when a discontinuity exists in the underlying intensity $I(t, z, \mu)$. This observation agrees with the numerical values shown in Table 4.1, where the L_2 and L_∞ errors are shown for various methods that all have the same degrees of freedom (DOF = 16).

Additionally, we study the profile of $E(t, z)$ for various methods in Figure 4.4. Each H_N^T solution in Figure 4.4 shows the propagation of multiple waves depending on the number of distinct eigenvalues of the matrix \mathbf{A} defined in (2.18) and (2.21). In particular, in Figure 4.4a and Figure 4.4b we compare H_N^1 and H_N^2 solutions with various N , respectively. Analogously, in Figure 4.4c and 4.4d we compare various H_1^T and H_2^T solutions with different T , respectively. Finally, in Figure 4.4e through 4.4h we plot in each panel a different H_N^T method with DOF = 16: (e) H_{15}^1 , (f) H_7^2 , (f) H_3^4 , and (g) H_1^8 . Again, we conclude from these simulations that in the case when the intensity is discontinuous, increasing T is more effective than increasing N . We also demonstrate in these panels that when T is odd and N is even (i.e., \mathbf{A} has a zero eigenvalue – see Remark 2.1), the solution degrades significantly: Figure 4.4a (H_2^1 and H_4^1) and in Figure 4.4d (H_2^1 and H_5^2).

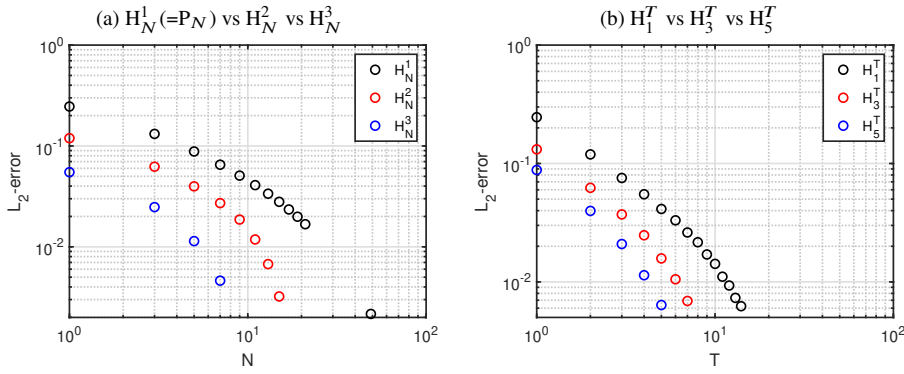


Fig. 4.3: (§4.2: Streaming in a vacuum) Convergence study of H_N^T solutions for the vacuum propagation problem at $t = 2.5 \times 10^{-11}$ s with $N_z = 100$ and CFL = 0.3 with respect to (a) N and (b) T .

error	H_1^8	H_3^4	H_7^2	$H_{15}^1 (= P_{15})$
L_2	2.1623×10^{-2}	2.4764×10^{-2}	2.7112×10^{-2}	2.7934×10^{-2}
L_∞	5.6687×10^{-2}	6.2532×10^{-2}	6.3653×10^{-2}	7.3359×10^{-2}

Table 4.1: (§4.2: Streaming in a vacuum) L_2 and L_∞ errors for the vacuum propagation problem for various methods that all have the same degrees of freedom (DOF = 16).

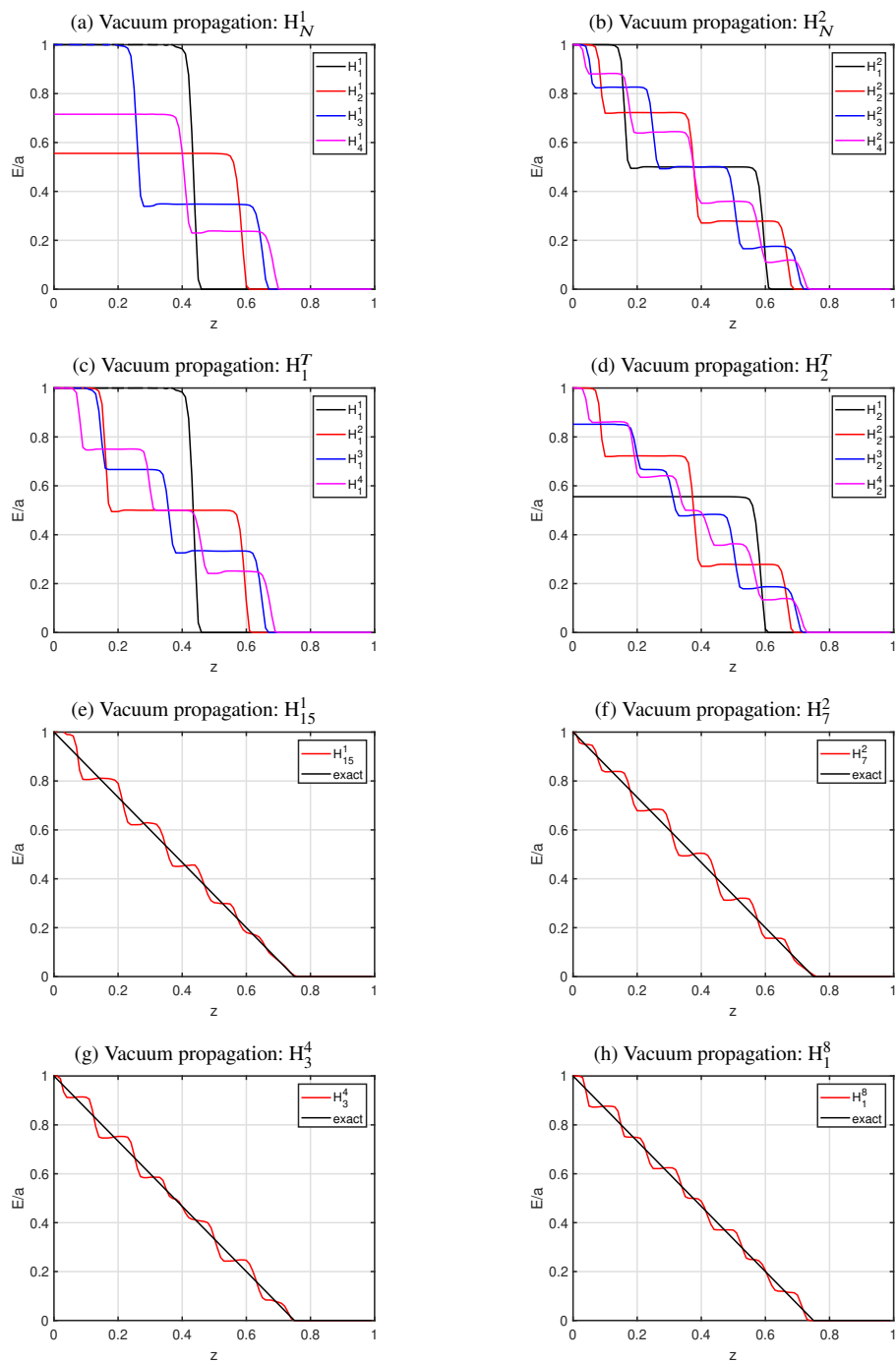


Fig. 4.4: (§4.2: Streaming in a vacuum) The H_N^T solutions for the vacuum propagation problem at $t = 2.5 \times 10^{-11}$ with $N_z = 100$ and CFL = 0.3.

4.3 Su-Olson problem

The next benchmark problem we solve is the non-equilibrium Su-Olson problem with material coupling [32]. In order to compare the numerical solutions to the semi-analytic solution, we follow the conditions used in [32], i.e., $\sigma = 1$, and the external source term is given by

$$S(t, z) = \begin{cases} ac & \text{if } -0.5 \leq z \leq 0.5, \\ 0 & \text{otherwise.} \end{cases} \quad (4.11)$$

We use the computational domain $z \in [-ct_{\text{end}} - 1, ct_{\text{end}} + 1]$ with periodic boundary conditions. For this problem, both $P_N = H_N^1$ and H_N^T perform very well even with small N .

Figure 4.5 shows the results from three different simulations with $ct_{\text{end}}=1.0, 3.16$, and 10.0 , respectively. The solutions to these three cases are shown on a linear scale in Figure 4.5a (P_3 and H_1^2) and 4.5b (P_5 and H_2^2), and on a log-log scale in Figure 4.5c (P_3 and H_1^2) and 4.5d (P_5 and H_2^2). The reference solutions are obtained from [32].

4.4 Diffusive Marshak-wave problem

In this section, a diffusive Marshak-wave problem is investigated; this problem is a standard test case in the literature [6, 19, 21, 34]. This problem consists of a semi-infinite medium of material with the opacity

$$\sigma = 300/\theta^3. \quad (4.12)$$

The computational domain is $z \in [0.0, 0.6]$ and the initial conditions are given by the following with $\theta_0 = 10^{-4}$ keV:

$$I(t=0, z, \mu) = \frac{1}{2}ac\theta_0^4 \quad \text{and} \quad \theta(t=0, z) = \theta_0. \quad (4.13)$$

We use the isotropic incoming boundary condition corresponding to a 1 keV temperature source on the left boundary $z_L = 0$, and no incoming radiation on the right boundary at $z_R = 0.6$:

$$I(t, z_L, \mu > 0) = \frac{1}{2}ac \quad \text{and} \quad I(t, z_R, \mu < 0) = 0. \quad (4.14)$$

We compute the material temperature, $\theta(t, z)$ at various times: $t = 10^{-8}$ s, 5×10^{-8} s, and 10^{-7} s. In our numerical tests for this problem all H_N^T solutions look similar, thus, we only present H_2^2 solutions in Figure 4.6. In this test, we use $N_z = 15$ with the mesh size $\Delta z = 0.04$. Despite the fact that we use a coarse mesh, the H_N^T solution is able to adequately capture the wave propagation front. Due to the fact that diffusion dominates, we are able to achieve stable results with a relaxed Courant number: CFL = 1.7. The reference solution shown in this plot is the semi-analytic equilibrium-diffusion solution (e.g., see [21]).

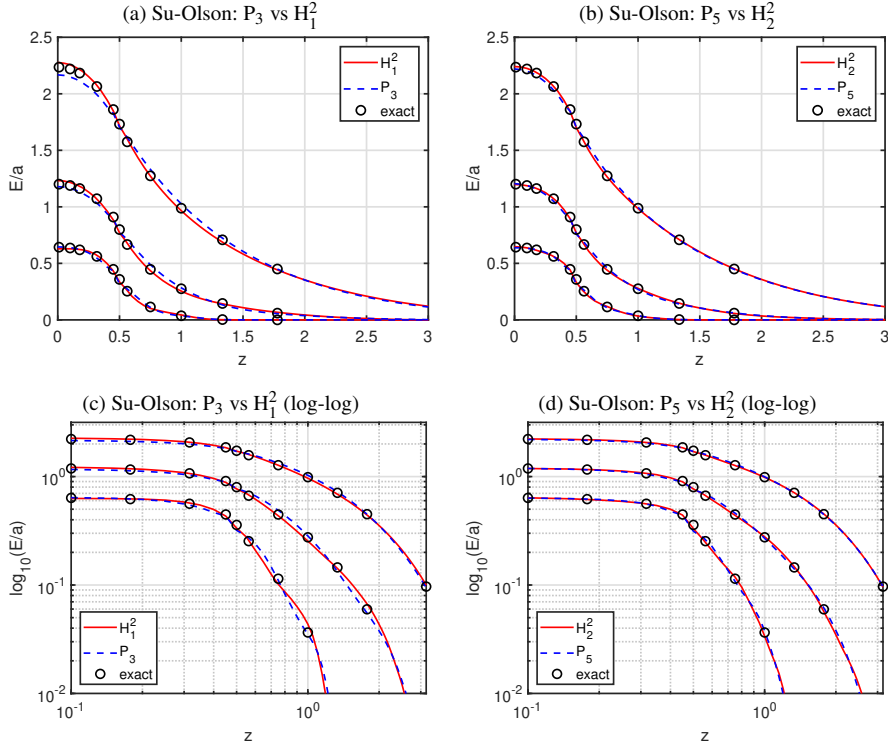


Fig. 4.5: (§4.3: Su-Olson problem) Three different simulations using H_N^T for the Su-Olson problem with $N_z = 100$, $\text{CFL} = 0.3$, and $ct_{\text{end}} = 1.0, 3.16, 10$, respectively. Panels (a) and (b) show P_3 , H_1^2 , P_5 , and H_2^2 on a linear scale, while panels (c) and (d) show those same solutions on a log-log scale.

4.5 Marshak-wave in thin medium

Here we apply our scheme to a Marshak-wave problem in an optically thin medium with an opacity given by

$$\sigma = 3/\theta^3. \quad (4.15)$$

The radiation temperature is given by

$$\theta_{\text{rad}}(t, z) := \sqrt[4]{\frac{E(t, z)}{a}}, \quad (4.16)$$

and the computational domain is $z \in [0, 0.35]$. We use the isotropic incoming boundary condition corresponding to a 1 keV temperature source on the left boundary $z_L = 0$, and no incoming radiation on the right boundary at $z_R = 0.35$:

$$I(t, z_L, \mu > 0) = \frac{1}{2}ac \quad \text{and} \quad I(t, z_R, \mu < 0) = 0. \quad (4.17)$$

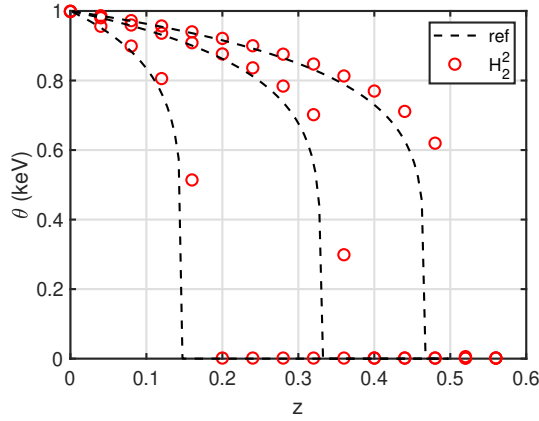


Fig. 4.6: (§4.4: Diffusive Marshak-wave problem) The H_2^2 solutions for the material temperature, $\theta(t, z)$, for the diffusive Marshak-wave problem at various times: $t = 10^{-8}$ s, 5×10^{-8} s, and 10^{-7} s, respectively, with $N_z = 15$, $\sigma = 300/\theta^3$, $\theta_0 = 10^{-4}$ keV, and CFL = 1.7. The reference solution is the semi-analytic equilibrium-diffusion solution.

The initial conditions are given by the following with $\theta_0 = 10^{-5}$ keV:

$$I(t=0, z, \mu) = \frac{1}{2}ac\theta_0^4 \quad \text{and} \quad \theta(t=0, z) = \theta_0. \quad (4.18)$$

In Figure 4.7a we show the H_2^2 solution with $N_z = 400$ for the material temperature, θ , and the radiation temperature, θ_{rad} (4.16). In Figure 4.7b we show the material temperature error for H_2^2 for various N_z . The error is computed by comparing the H_2^2 solutions with various N_z to the P_5 solution with $N_z = 2048$. This figure shows the expected degradation of the order of accuracy to first order in space for this problem due to the discontinuity of the solution.

Furthermore, in Figure 4.8 we investigate the various convergence rates of H_N^1, H_N^2, H_N^4 and H_N^8 with $N_z = 512$ as a function of N . In particular, we compute the following approximate L_2 error:

$$L_2 \text{ error} := \left[\frac{0.35}{N_z} \sum_{i=1}^{N_z} \left(\theta_{2j-1}^T(t_{\text{end}}, z_i) - \theta_{99}^T(t_{\text{end}}, z_i) \right)^2 \right]^{1/2}, \quad (4.19)$$

for $j = 1, 2, \dots, 9$, where θ_N^T represents the material temperature as calculated with the H_N^T model. Due to the non-smoothness of the solution we note a fairly rapid convergence as a function of T with fixed N , and slower convergence as a function of N with fixed T .

4.6 Smooth Marshak-wave

Finally, a smooth Marshak-wave problem is considered in this section to observe the convergence rate of our numerical scheme on a smooth solution in an optically

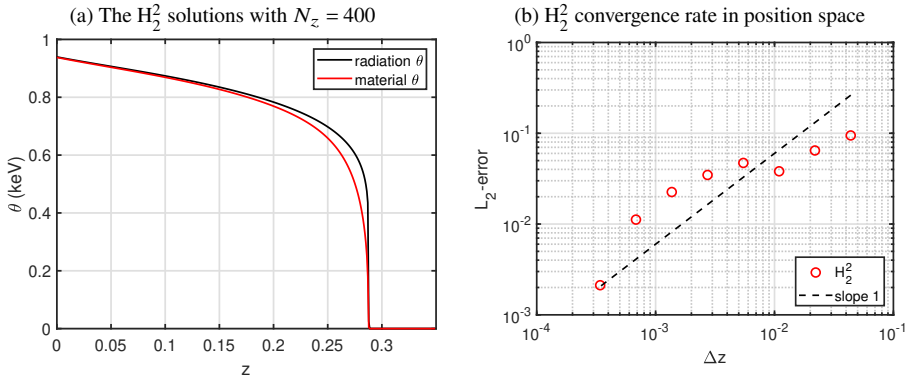


Fig. 4.7: (§4.5: Marshak-wave in thin medium) The H_2^2 solutions and convergence rate for the thin Marshak-wave problem at $t = 10^{-9}$ s with $\sigma = 3/\theta^3$, $\theta_0 = 10^{-5}$ keV, and CFL = 0.3.

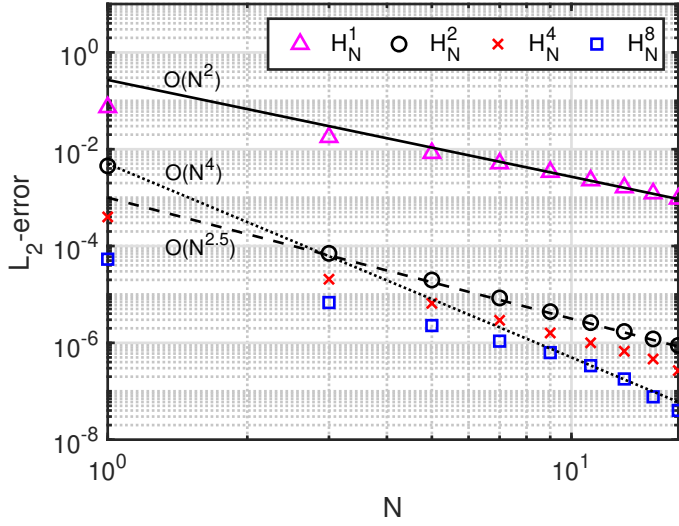


Fig. 4.8: (§4.5: Marshak-wave in thin medium) Error in various H_N^T approximations with $N_z = 512$ and CFL = 0.3.

thin medium. The opacity and radiation temperatures are again given by (4.15) and (4.16), respectively. Following [20,21], the computational domain is $z \in [0, 0.8]$ and the smooth initial conditions are given by:

$$I(t=0, z, \mu) = \frac{ac}{2} \left[1 - 0.498 \left(1 + \tanh [50(z - 0.25)] \right) \right], \quad (4.20)$$

$$\theta(t=0, z) = \left(\frac{E(t=0, z)}{a} \right)^{\frac{1}{4}}. \quad (4.21)$$

The boundary conditions are given by

$$I(t, z_L, \mu > 0) = I(t = 0, z_L, \mu) \quad \text{and} \quad I(t, z_R, \mu < 0) = 0, \quad (4.22)$$

where $z_L = 0$ and $z_R = 0.8$.

In Figure 4.9 we show the solution for the material temperature, $\theta(t, z)$, at various times: (a)

The initial condition for the material temperature, $\theta(t, z)$, is shown in Panel (a) of Figure 4.9. In Figure 4.9(b) we show a direct comparison of the material temperature as computed with P_5 and H_2^2 , both methods have $\text{DOF} = 6$, for $N_z = 128$. In Figure 4.9(c) and Figure 4.9(d) we show the material temperature as computed by P_5 and H_2^2 with various N_z , respectively.

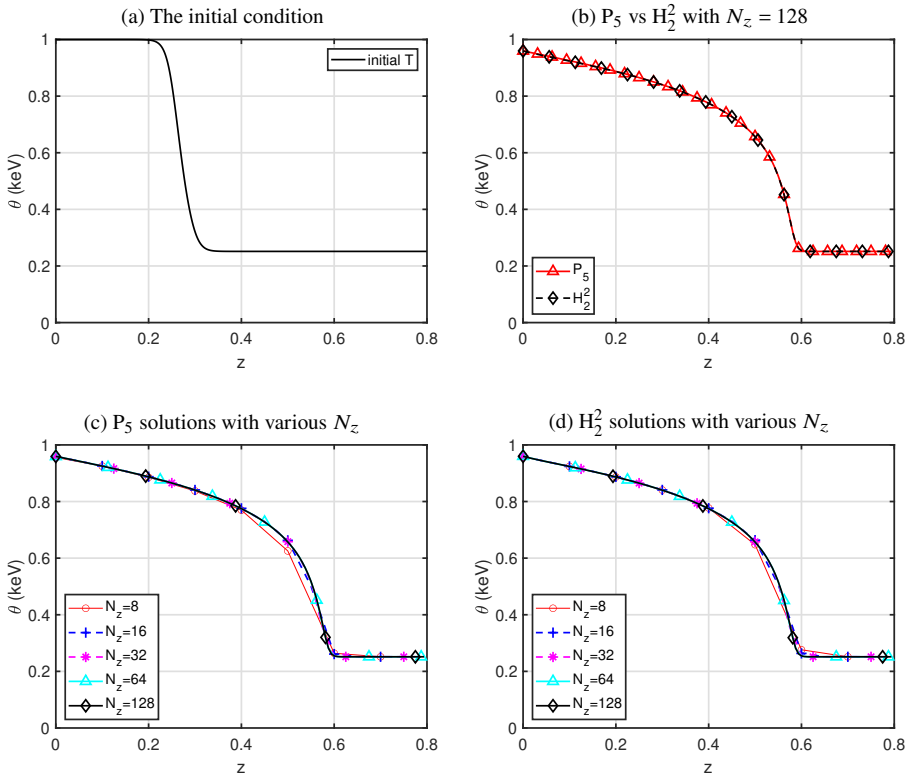


Fig. 4.9: (§4.6: Smooth Marshak-wave) Comparison of the P_5 and H_N^2 solutions for the material temperature for the smooth Marshak wave problem with $\text{CFL} = 0.3$.

Finally, in Figure 4.10 we demonstrate second-order convergence of the H_2^2 with increasing mesh resolution N_z . In this figure, the dashed-line indicates a slope of two on a log-log scale. In these convergence experiments the approximate L_2 error is

calculated via the formula:

$$L_2(\theta - \theta^{2048}) := \sqrt{\frac{0.8}{N_z} \sum_{k=1}^{N_z} \left(\theta_k - \theta_k^{2048/(2^m)} \right)^2}, \quad (4.23)$$

where

$$\theta_k^{2048/(2^{m+1})} = \frac{1}{2} \left(\theta_{2^{(k-1)+1}}^{2048/(2^m)} + \theta_{2^{(k-1)+2}}^{2048/(2^m)} \right), \quad (4.24)$$

for $m = 0, 1, \dots, 7$. Here θ^{2048} represents the reference temperature solution on mesh with $N_z = 2048$ cells, and the superscript k stands for the k^{th} grid cell. The idea encapsulated in formulas (4.23) and (4.24) is that we project the reference solution θ^{2048} onto coarser mesh, i.e., $N_z = 2048/(2^m)$, for $m = 1, 2, \dots, 8$ by taking the average of left and right cell on finer mesh, to obtain $\theta^{1024}, \theta^{512}, \dots, \theta^8$; once we have projected this solution down to the mesh on which θ is defined, we can directly compute the L_2 distance. In Figure 4.10 we have used this strategy with $N_z = 8, 16, 32, 64, 128, 256, 512, \text{ and } 1024$ to show the convergence rate.

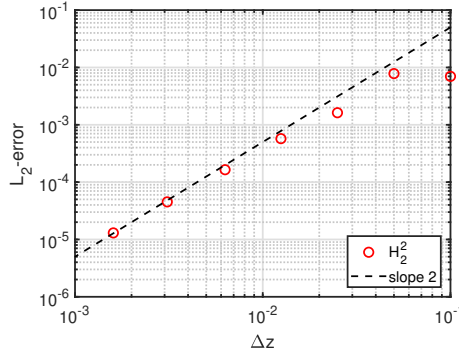


Fig. 4.10: (§4.6: Smooth Marshak-wave) Convergence rate of the material temperature θ for the smooth Marshak wave problem.

5 Conclusion

In this work we have developed the hybrid discrete (H_N^T) approximation method for the thermal radiative transfer (TRT) equations, and implemented a numerical discretization of these equations using a second order discontinuous Galerkin finite element method in conjunction with a semi-implicit time-stepping scheme. The H_N^T approach acquires desirable properties of two classical methods for the TRT equations, namely P_N (spherical harmonics) and S_N (discrete ordinates), and indeed reduces to each of these approximations in various limits: $H_N^1 \equiv P_N$ and $H_0^T \equiv S_T$. We proved that the H_N^T approximation results in a system of hyperbolic partial differential equations for all $T \geq 1$ and $N \geq 0$. In particular, in one spatial dimension, the H_N^T

scheme is essentially a collection of P_N approximations localized in each velocity band. Because of this structure, H_N^T , just like P_N , can exhibit negative densities. However, because H_N^T has band-localized structure, we are able to control unphysical numerical oscillations by increasing the number of discrete regions in velocity space, thereby blending properties of P_N and S_N .

Once the H_N^T approximation was developed for TRT, we introduced a semi-implicit numerical method that is based on a second order explicit Runge-Kutta scheme for the streaming term and an implicit Euler scheme for the material coupling term. Furthermore, in order to solve the material energy equation implicitly after each predictor and corrector step, we linearized the temperature term using a Taylor expansion; this avoided the need for an iterative procedure, and therefore improved efficiency. In order to reduce unphysical oscillation, we applied a slope limiter after each time step.

In the numerical results section we compared the solutions of the H_N^T and P_N schemes for the various benchmark problems. We demonstrated for a variety of problems that for a fixed total number of moments, we are able to achieve accuracy gains over the $P_N \equiv H_N^1$ approximation by balancing T and N . With a more balanced choice of T and N , H_N^T shows less oscillation than P_N , especially in the presence of discontinuities.

In future work, we will develop extensions of the H_N^T method for multi-energy group models or frequency-dependent equations in multiple dimensions. In particular, just as we have done in this work, we will investigate various choices of N and T to achieve accurate and efficient moment closure in the multidimensional setting. We will also investigate adaptive strategies for selecting T and N in the presence of some appropriate error indicator.

Acknowledgements JAR was supported in part by NSF Grants DMS-1620128 and DMS-2012699.

References

1. Adams, M.P., Adams, M.L., Hawkins, W.D., Smith, T., Rauchwerger, L., Amato, N.M., Bailey, T.S., Falgout, R.D., Kunen, A., Brown, P.: Provably optimal parallel transport sweeps on semi-structured grids. *J. Comput. Phys.* **407**, 109–234 (2020)
2. Brunner, T.A., Holloway, J.P.: Two-dimensional time-dependent Riemann solvers for neutron transport. *J. Comput. Phys.* **210**(1), 386–399 (2005)
3. Carlson, B.: Solution of the transport equation by the S_N method. Los Alamos National Laboratory (1955)
4. Carlson, B.: Tables of symmetric equal weight quadrature EQn over the unit sphere. Los Alamos National Laboratory (1971)
5. Cohen, A.: An algebraic approach to certain differential eigenvalue problems. *Linear Algebra Appl.* **240**, 183–198 (1996)
6. Evans, T.M., Urbatsch, T.J., Lichtenstein, H., Morel, J.E.: A residual Monte Carlo method for discrete thermal radiative diffusion. *J. Comput. Phys.* **189**(2), 539–556 (2003)

7. Fan, Y.W., Li, R., Zheng, L.C.: A Nonlinear Moment Model for Radiative Transfer Equation in Slab Geometry. *J. Comput. Phys.* **404**, 109–128 (2020)
8. Fleck, J.A., Jr., Cummings, J.D.: An implicit Monte Carlo scheme for calculating time and frequency dependent nonlinear radiation transport. *J. Comput. Phys.* **8**(3), 313–342 (1971)
9. Hauck, C.D., McClarren, R.G.: Positive P_N closures. *SIAM J. Sci. Comput.* **32**(5), 2603–2626 (2010)
10. Jarrell, J., Adams, M.: Discrete-ordinates quadrature sets based on linear discontinuous finite elements. In: *Proc. International Conference on Mathematics and Computational Methods applied to Nuclear Science and Engineering*, Rio de Janeiro, Brazil (2011)
11. Klar, A.: An asymptotic-induced scheme for nonstationary transport equations in the diffusive limit. *SIAM J. Numer. Anal.* **35**(3), 1073–1094 (1998)
12. Klar, A., Unterreiter, A.: Uniform stability of a finite difference scheme for transport equations in diffusive regimes. *SIAM J. Numer. Anal.* **40**(3), 891–913 (2002)
13. Koch, R., Krebs, W., Wittig, S., Viskanta, R.: The discrete ordinate quadrature schemes for multidimensional radiative transfer. *J. Quant. Spectrosc. Ra.* **53**(4), 353–372 (1995)
14. Lathrop, K.D.: Ray effects in discrete ordinates equations. *Nucl. Sci. Eng.* **32**(3), 357–369 (1968)
15. Lathrop, K.D.: Remedies for ray effects. *Nucl. Sci. Eng.* **45**(3), 255–268 (1971)
16. Lathrop, K.D., Carlson, B.G.: Discrete ordinates angular quadrature of the neutron transport equation. Los Alamos Scientific Laboratory Report 3186 (1965)
17. Lau, C., Adams, M.: Discrete Ordinates Quadratures Based on Linear and Quadratic Discontinuous Finite Elements over Spherical Quadrilaterals. *Nucl. Sci. Eng.* **185**(1), 36–52 (2017)
18. Lewis, E.E., Miller, W.F.: *Computational Methods of Neutron Transport*. John Wiley & Sons, DeKalb (1994)
19. Li, W., Liu, C., Zhu, Y., Zhang, J., Xu, K.: Unified gas-kinetic wave-particle methods III: Multiscale photon transport. *J. Comput. Phys.* **408**, 109–280 (2020)
20. Lowrie, R.B.: A Comparison of Implicit Time Integration Methods for Nonlinear Relaxation and Diffusion. *J. Comput. Phys.* **196**(2), 566–590 (2004)
21. McClarren, R.G., Evans, T.M., Lowrie, R.B., Densmore, J.D.: Semi-implicit time integration for P_N thermal radiative transfer. *J. Comput. Phys.* **227**(16), 7561–7586 (2008)
22. McClarren, R.G., Holloway, J.P., Brunner, T.A.: On solutions to the pn equations for thermal radiative transfer. *Journal of Computational Physics* **227**(5), 2864–2885 (2008)
23. McClarren, R.G., Lowrie, R.B.: The effects of slope limiting on asymptotic-preserving numerical methods for hyperbolic conservation laws. *J. Comput. Phys.* **227**(23), 9711–9726 (2008)
24. McClarren, R.G., Urbatsch, T.J.: A modified implicit monte carlo method for time-dependent radiative transfer with adaptive material coupling. *Journal of Computational Physics* **228**(16), 5669–5686 (2009)
25. Olson, G.: Second-order time evolution of P_N equations for radiation transport. *J. Comput. Phys.* **228**(8), 3072–3083 (2009)

26. Olson, G.L., Auer, L.H., Hall, M.L.: Diffusion, p_1 , and other approximate forms of radiation transport. *J. Quant. Spectrosc. Ra.* **64**(6), 619–634 (2000)
27. Parlett, B.N.: *The Symmetric Eigenvalue Problem*. Prentice-Hall Series in Comput. Math. **61**(7), 277–348 (1981)
28. Pomraning, G.C.: Variational boundary conditions for the spherical harmonics approximation to the neutron transport equation. *Ann. Phys.* **27**, 193–215 (1964)
29. Pomraning, G.C.: *The Equations of Radiation Hydrodynamics*. Pergamon Press, Oxford, U.K. (1973)
30. Shin, M.: Hybrid discrete (H_N^T) approximations to the equation of radiative transfer. Ph.D. thesis, Iowa State University, Ames, IA (2019)
31. Siegel, R., Howell, J.R.: *Thermal radiation heat transfer*, vol. 3. Hemisphere Publishing Corp., Washington, United States (1972)
32. Su, B., Olson, G.L.: An analytical benchmark for non-equilibrium radiative transfer in an isotropically scattering medium. *Ann. Nucl. Energy* **24**(13), 1035–1055 (1997)
33. Thurgood, C.P., Pollard, A., Becker, H.A.: The T_N Quadrature Set for the Discrete Ordinates Method. *J. Heat Transfer* **117**(4), 1068–1070 (1995)
34. Vikas, V., Hauck, C., Wang, Z., Fox, R.: Radiation transport modeling using extended quadrature method of moments. *J. Comput. Phys.* **246**(1), 221–241 (2013)
35. Wikipedia: Gaussian quadrature (2021). URL https://en.wikipedia.org/wiki/Gaussian_quadrature
36. Wollaber, A.B.: Four decades of implicit monte carlo. *Journal of Computational and Theoretical Transport* **45**(1-2), 1–70 (2016)